

Spin dynamics and unconventional magnetism in insulating $\text{La}_{(1-2x)}\text{Sr}_{2x}\text{Co}_{(1-x)}\text{Nb}_x\text{O}_3$

Rishabh Shukla,¹ Anil Jain,² M. Miryala,³ M. Murakami,³ K. Ueno,³ S. M. Yusuf,^{2,4} and R. S. Dhaka^{1,*}

¹*Department of Physics, Indian Institute of Technology Delhi, Hauz Khas, New Delhi-110016, India*

²*Solid State Physics Division, Bhabha Atomic Research Centre, Mumbai-400085, India*

³*Shibaura Institute of Technology, Toyosu campus, Koto-ku Tokyo, Japan*

⁴*Homi Bhabha National Institute, Anushaktinagar, Mumbai-400094, India*

(Dated: June 11, 2019)

We study the structural, magnetic, transport and electronic properties of LaCoO_3 with Sr/Nb co-substitution, i.e., $\text{La}_{(1-2x)}\text{Sr}_{2x}\text{Co}_{(1-x)}\text{Nb}_x\text{O}_3$ using x-ray and neutron diffraction, dc and ac-magnetization, neutron depolarization, dc-resistivity and photoemission measurements. The powder x-ray and neutron diffraction data were fitted well with the rhombohedral crystal symmetry (space group $R\bar{3}c$) in Rietveld refinement analysis. The calculated effective magnetic moment ($\approx 3.85 \mu_B$) and average spin (≈ 1.5) of Co ions from the analysis of magnetic susceptibility data are consistent with 3+ state of Co ions in intermediate-spin (IS) and high-spin (HS) states in the ratio of $\approx 50:50$, i.e., spin-state of Co^{3+} is preserved at least up to $x = 0.1$ sample. Interestingly, the magnetization values were significantly increased with respect to the $x = 0$ sample, and the M-H curves show non-saturated behavior up to an applied maximum magnetic field of ± 70 kOe. The ac-susceptibility data show a shift in the freezing temperature with excitation frequency and the detailed analysis confirm the slower dynamics and a non-zero value of the Vogel-Fulcher temperature T_0 , which suggests for the cluster spin glass. The unusual magnetic behavior indicates the presence of complex magnetic interactions at low temperatures. The dc-resistivity measurements show the insulating nature in all the samples. However, relatively large density of states $\approx 10^{22} \text{ eV}^{-1} \text{ cm}^{-3}$ and low activation energy ≈ 130 meV are found in $x = 0.05$ sample. Using x-ray photoemission spectroscopy, we study the core-level spectra of La 3d, Co 2p, Sr 3d, and Nb 3d to confirm the valence state.

INTRODUCTION

The spin-state transition present in the LaCoO_3 is an open question for the researchers even after enormous theoretical as well as experimental efforts since many decades [1–7]. In LaCoO_3 , Co is in Co^{3+} ($3d^6$) state and their ground state is characterized by the low spin electronic configuration [LS; $S=0$; $t_{2g}^6 e_g^0$], whereas other excited states are defined as intermediate spin state (IS; $S=1$; $t_{2g}^5 e_g^1$) and high spin state (HS; $S=2$; $t_{2g}^4 e_g^2$). The ground state of LaCoO_3 gradually passes to IS, HS or mixed state of IS/HS with temperature, pressure, magnetic field, cationic substitution as well as with induced lattice strain [4, 8–23]. The energy difference between LS and IS state of the Co^{3+} ion is rather small (~ 80 K in temperature scale), usually this energy difference increases with the reduction of CoO_6 octahedron volume and vice versa [24], however above 80 K, Co ion is found in IS configuration showing Jahn-Teller (JT) distortion [2]. The Co^{3+} possess larger ionic radius in IS state (0.56 \AA) than in the LS state (0.545 \AA) [25–27]; therefore, an increase in unit cell volume favors transition from LS to IS state. The second transition at 500 K is attributed to an insulator to metal transition. The band structure calculations within the LDA+U approximation demonstrated that the IS state is lowest in energy after the first transition [2, 28]. In contrast to the expectation from the simple ionic model, IS is stabilized by a strong p-d hybridization and possible orbital ordering in the e_g shell of Co^{3+} ions [2]. The redistribution of electrons between the t_{2g} and e_g levels results from a com-

petition between the crystal field splitting energy (Δ_{CF}) and the intra-atomic Hund's exchange energy (J_{ex}); however, both terms have comparable values in cobaltites. The crystal field splitting energy strongly depends on the Co-O bond length, therefore in a pure ionic picture the ground state is stabilized with $\Delta > 3J_{ex}$ and for HS state $\Delta < 3J_{ex}$. The competition between Δ and J_{ex} can easily be controlled by cationic substitution either at La or Co site [8, 15]. This has been observed in the behavior of $\text{LaCo}_{1-x}\text{Rh}_x\text{O}_3$ and $\text{La}_{1-x}\text{Sr}_x\text{CoO}_3$, in which the spin state transition disappears for certain compositions and Co ions remain/retain magnetic down to the lowest measured temperature [29, 30].

The Sr^{2+} ionic radius (1.44 \AA) is significantly greater than that of the La^{3+} ion (1.36 \AA), so it is possible to anticipate that the stabilization of IS state of Co ions by substituting Sr^{2+} ions at La^{3+} site [31]. We believe that Sr ions, whose radius is larger than that of La ions, increase the average Co-O distance in part of the CoO_6 octahedra, which favors transition of the Co^{3+} ions from the LS to IS state. However, at such heterovalent substitution Co^{4+} ions appear, leading to the ferromagnetic metallic ground state [30, 32, 33]. The majority of researchers intended that ferromagnetism in cobaltites attribute to the phenomenon of double exchange interaction (between Co^{3+} – Co^{4+}), as comprehended in manganites [34, 35]. Other interesting case is that the hole doping (Ca, Sr, Ba at La site) in LaCoO_3 drives the system in metallic regime whereas the substitution of Nb at Co site impels towards the insulating regime [7]. Therefore, the co-substitution of both cations on their respective sites

in LaCoO_3 would alter its transport behavior. It is well reported that regardless of having larger ionic radii, Sr^{2+} does not induce any structural transformation in the system up to 50% concentration [36]. Whereas, our recent study reveals that the Nb^{5+} substitution at Co site induces structural transformation of lower symmetry from the rhombohedral to orthorhombic, and then monoclinic at higher concentration [7].

Here, we have simultaneously substituted Sr and Nb in place of La and Co in a ratio of 2:1, respectively. The substitution of Sr^{2+} at La^{3+} site changes the Co ion from Co^{3+} to Co^{4+} , and the substitution of one Nb^{5+} at Co site converts two Co^{3+} into the Co^{2+} ions [7, 30]. Therefore with co-substitution of Sr and Nb in 2:1 ratio, the valence state of Co ion can be maintained in 3+. In order to understand the effect of co-substitution in $\text{La}_{(1-2x)}\text{Sr}_{2x}\text{Co}_{(1-x)}\text{Nb}_x\text{O}_3$, we study the structural, magnetic, transport and electronic properties. The Rietveld refinement of x-ray and neutron diffraction data reveal the rhombohedral symmetry for all the samples and an increase in the unit cell volume with higher substitution. The derived values of effective magnetic moment confirm the 3+ valence state of Co ions, which is consistent as co-substitution is expected to maintain Co ions in 3+ state. We further confirm the valence state of Co ion using photoemission spectroscopy. The extracted characteristic frequency from ac-susceptibility data exhibits slower spin dynamics of the system and suggests that the origin of spin glass state is not from individual spins rather related to their clusters. The transport properties manifest that co-substitution drives system towards the insulating regime; fitted data for the possible conduction mechanisms provide the values of activation energy as well as density of states near the Fermi level.

EXPERIMENTAL

Polycrystalline samples of $\text{La}_{(1-2x)}\text{Sr}_{2x}\text{Co}_{(1-x)}\text{Nb}_x\text{O}_3$ were synthesized by the conventional solid state solution method. We used strontium carbonate (SrCO_3), cobalt oxide (Co_3O_4) and niobium oxide (Nb_2O_5) as purchased, whereas purchased lanthanum oxide (La_2O_3) powder was dried at 700 °C for 12 hrs prior to use. Stoichiometric amount of starting materials (all $\geq 99.9\%$ from Sigma/Alfa) were thoroughly mixed with the help of mortar-pestle and reacted at 1100°C for 12 hrs in air, pellets of calcined powder were cold pressed at 2000 psi and sintered in air at 1475°C for 6 – 10 hrs [7, 37].

X-ray diffraction data were collected with a $\text{CuK}\alpha$ radiation ($\lambda = 1.5406 \text{ \AA}$) using Panalytical x-ray diffractometer, magnetic and transport measurements were done with physical property measurement system (PPMS) from Quantum Design, USA. Ac-susceptibility measurements were carried out in a CRYOGENIC make, liquid He based PPMS at BARC, India. We analyzed the

XRD data by Rietveld refinement using FullProf package and the background was fitted using the linear interpolation between the data points. We recorded the powder neutron diffraction data at temperatures 3 and 300 K for bulk $\text{La}_{(1-2x)}\text{Sr}_{2x}\text{Co}_{(1-x)}\text{Nb}_x\text{O}_3$ ($x = 0.025, 0.05,$ and 0.15) samples, using the powder diffractometer PD-I ($\lambda = 1.094 \text{ \AA}$) at the Dhruva reactor, Trombay, Mumbai, India. One dimensional neutron depolarization measurements over the temperature range of 4–300 K, to identify the ferromagnetic clusters, were carried out using the polarized neutron spectrometer (PNS) at the Dhruva reactor, under an applied magnetic guide field of 50 Oe. For the neutron depolarization measurements, polarized neutrons ($\lambda = 1.205 \text{ \AA}$) were produced and analyzed by using magnetized Cu_2MnAl (111) and $\text{Co}_{0.92}\text{Fe}_{0.08}$ (200) single crystals, respectively. The two different states (up and down) of the incident neutron beam polarization were achieved by a π flipper just before the sample. The polarization of the neutron beam was determined by measuring the intensities of neutrons in non-spin flip and spin flip channels with the flipper off and on (flipping ratio, R), respectively. The core-level spectra of La 3d, Co 2p, Sr 3d and Nb 3d were recorded at room temperature using a monochromatic Al-K α source (energy resolution = 0.5 eV), in a base pressure of 5×10^{-10} mbar. We used a charge neutralizer to compensate the charging effect in these insulating samples.

RESULTS AND DISCUSSION

A. Room temperature x-ray and neutron diffraction

The crystal structure of $\text{La}_{(1-2x)}\text{Sr}_{2x}\text{Co}_{(1-x)}\text{Nb}_x\text{O}_3$ samples has been investigated by the Rietveld refinement of both x-ray and neutron diffraction data measured at room temperature. The lattice parameters were determined from the refinement of x-ray diffraction (XRD) patterns and were used as a starting point for the refinement of neutron diffraction (ND) data. Due to sensitivity of neutron towards lighter atom, the positions of oxygen were obtained from the refinement of neutron diffraction data and were kept fix during the final stage refinement of x-ray diffraction data. The Rietveld refined x-ray and neutron diffraction patterns are presented in Figures 1 and 2, respectively. The refinement confirms single phase formation of these samples in rhombohedral structure (space group $R\bar{3}c$ #167). The Rietveld refined lattice parameters and unit cell volume show systematic increment with increasing the amount of substitution, as presented in table I. Also, in table I, we present pseudocubic (pc) lattice parameters calculated using $a_{pc} = a/\sqrt{2}$, $b_{pc} = b/\sqrt{2}$, $c_{pc} = c/\sqrt{12}$, and unit cell volume (V_{pc}) for $\text{La}_{(1-2x)}\text{Sr}_{2x}\text{Co}_{(1-x)}\text{Nb}_x\text{O}_3$. Recently, it has been reported that the Nb substitution at Co site in LaCoO_3 induces the structural transition [7, 37], which can be

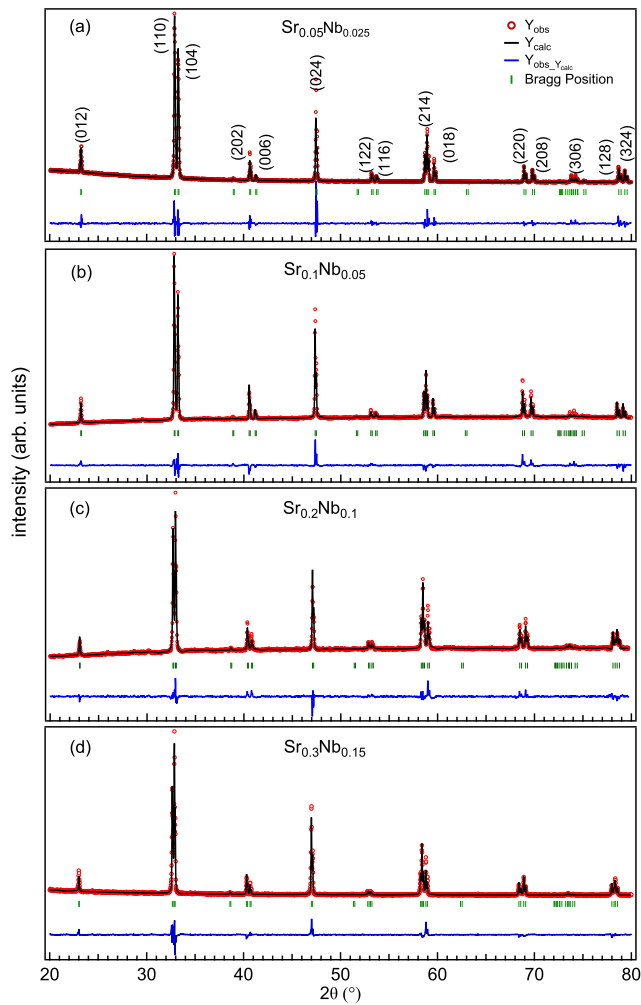


Figure 1. Rietveld refined powder x-ray diffraction data of $\text{La}_{(1-2x)}\text{Sr}_{2x}\text{Co}_{(1-x)}\text{Nb}_x\text{O}_3$ samples, (a) $x = 0.025$, (b) $x = 0.05$, (c) $x = 0.1$, and (d) $x = 0.15$. The Rietveld refinement profiles, the fitted Bragg peak positions, and the residual are shown in black solid lines, short vertical bars and blue lines in the bottom of each panel, respectively.

attributed to the difference in the ionic radius of Nb^{5+} and Co^{3+} ions. In LaCoO_3 , Co^{3+} ions have ionic radii of 0.545 Å in LS state and 0.61 Å in HS state, but Nb^{5+} ions have ionic radii of 0.64 Å [26, 27]. Due to the larger ionic radii of Nb ions, volume of octahedra around Co site increases and results in the modification of crystal structure. On the other hand, larger Sr^{2+} substitution at La site in LaCoO_3 will not change the structure up to $x = 0.5$ [36]. Therefore, the co-substitution of Sr^{2+} and Nb^{5+} in LaCoO_3 may generate the possibility of structural modification attributed to the perturbation of volume of polyhedra around both the sites. However, we observe that with co-substitution up to $x = 0.15$, there is no structural transition and we were able to fit the XRD and ND data with the rhombohedral space group $R\bar{3}c$ only, as clearly visible in Figures 1 and 2.

In Figures 2(a–c) we show the Rietveld refined powder neutron diffraction patterns measured at 300 K for the $x = 0.025, 0.05,$ and 0.15 samples, respectively. All the observed patterns were fitted by considering only the nuclear phase. In ABO_3 type perovskites the A site has cuboctahedral symmetry and here it has three groups of La–O bond-lengths, namely small (3 fold degenerate), intermediate (6 fold degenerate) and long (3 fold degenerate). The Rietveld refined parameters like bond-lengths and bond-angles from the Neutron diffraction for $\text{La}_{(1-2x)}\text{Sr}_{2x}\text{Co}_{(1-x)}\text{Nb}_x\text{O}_3$ are summarized in table I. We found that the long bond decreases, while

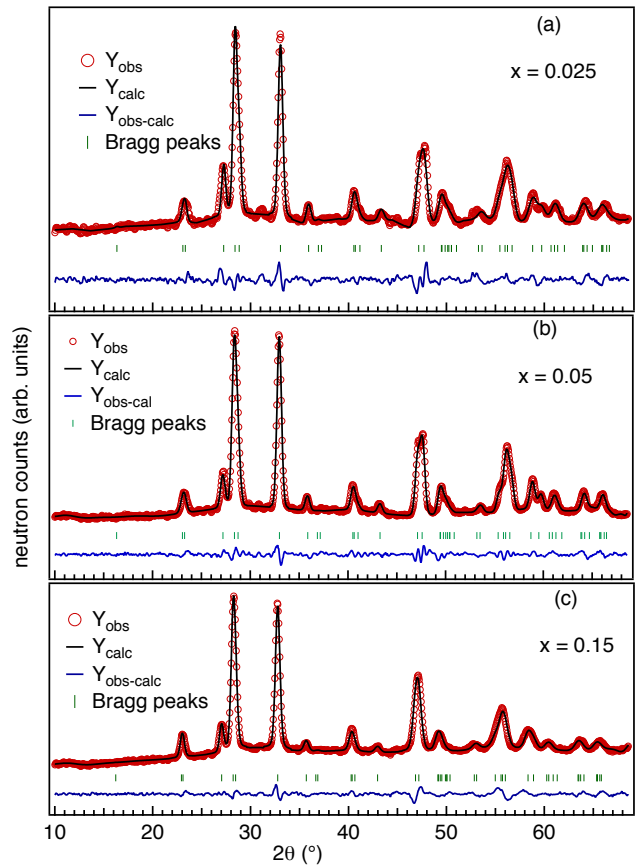


Figure 2. Rietveld refined neutron powder diffraction data for the $\text{La}_{(1-2x)}\text{Sr}_{2x}\text{Co}_{(1-x)}\text{Nb}_x\text{O}_3$ samples, (a) $x = 0.025$, (b) $x = 0.05$, and (c) $x = 0.15$, measured at room temperature. The Rietveld refinement profiles, the fitted Bragg peak positions, and the residual are shown in black solid lines, short vertical bars and blue lines in the bottom of each panel, respectively.

the other two groups of bonds increases with the substitution. This indicates that the long-bond compensate the effect of substitution of larger cations to preserve the crystal structure similar to the parent ($x = 0$) sample. The B site has an octahedral symmetry and sixfold degenerate Co–O bonds. Here the Co–O bond length increases and slightly larger than LaCoO_3 (1.934 Å) at 300 K [25], while the octahedra changes its bond-angles

Table 1. The Rietveld refined parameters of $\text{La}_{(1-2x)}\text{Sr}_{2x}\text{Co}_{(1-x)}\text{Nb}_x\text{O}_3$ samples; the lattice parameters and unit cell volume obtained from XRD analysis; the bond-lengths and bond-angles obtained from neutron diffraction, measured at 300 K.

XRD	χ^2	R_p	R_{wp}	a=b(Å)	c (Å)	V(Å ³)	$a_{pc}=b_{pc}$	c_{pc}	V_{pc}
x (%)		(%)	(%)				(Å)	(Å)	(Å ³)
0	1.75	3.31	4.57	5.4416(13)	13.0900(2)	335.679(9)	3.848	3.778	55.95
2.5	4.19	4.16	6.85	5.4449(13)	13.1195(4)	336.841(15)	3.850	3.783	56.14
5	3.2	3.52	5.35	5.4554(13)	13.1448(4)	338.801(15)	3.858	3.805	56.64
10	2.3	2.91	4.33	5.4766(16)	13.2594(5)	344.407(19)	3.871	3.841	57.55
15	2.8	4.21	6.23	5.4816(12)	13.2996(3)	346.087(14)	3.899	3.869	58.82

neutron	χ^2	R_p	R_{wp}	Co-O (Å)	Co-O-Co	O-Co-O	La-O (Å)	La-O (Å)	La-O (Å)	La-Co (Å)	La-Co (Å)
x (%)		(%)	(%)	×6	×3	×3	×3	×3	×6	×2	×6
2.5	2.27	1.42	2.0	1.9439(2)	163.029(1)	91.225(5)	3.0204(2)	2.4467(2)	2.7196(2)	3.2924(4)	3.3420(2)
5	4.85	1.84	2.77	1.9440(1)	164.465(3)	91.052(6)	2.9996(2)	2.4741(2)	2.7239(3)	3.3047(4)	3.3467(2)
15	2.28	1.52	2.03	1.9554(1)	165.693(1)	90.817(6)	2.9963(2)	2.5093(2)	2.7455(2)	3.3381(4)	3.3678(2)

i.e., O–Co–O decreases with the substitution.

Octahedral distortions are reflected in the tilting of BO_6 from the vertical axis and defined as $\phi_1 = (180 - \Theta)/2$, where Θ is defined as B–O–B bond angle along the z-axis. The tilting of octahedra is also quantified through the pseudo-cubic parameters c_{pc} and a_{pc} , defined as $c/\sqrt{12}$ and $a/\sqrt{2}$, respectively. The distortion parameter Δ_d is defined as $(1/12)\sum_{n=1-12} [(d_n - d_{avg})/d_{avg}]^2$, where d_{avg} is average bond length of La–O. The calculated values of Δ_d for the cuboctahedra are presented in table 2, where we can see that the tetragonal strain decreases with increasing the substitution. In order to obtain the information about the oxidation state of metal ion, we have calculated bond valence sum (BVS) from the bond-lengths of the octahedra without any assumptions. The BVS is generally calculated using an empirical relation based on the Pauling’s “2nd Rule” of electrostatic valence, which postulates that the total strength of the valence bond, which reaches an ion from all the surrounding atoms is equal to the charge of the ion [38, 39].

$$V_j = \sum_j s_{ij}$$

where the sum is over neighboring j atoms with each bond between atoms i and j having bond valence s_{ij} . Brown and Altermatt suggested the exponential form in 1985 [40] $s_{ij} = [\exp(R_0 - R_{ij})/b]$, where R_0 is termed as unit valence bond-length, and therefore a unique value for each metal-ion pair was tabulated. Here, R_{ij} is the experimentally observed bond-length between the ij metal-ion pair and b is an empirical constant, generally taken as 0.37 [41]. The bond valence parameter (R_0) depends on the metal-ion pair, valency of metal ion and the coordination number of the metal ion. The calculated BVS values from room temperature neutron data are presented in the table 2 for $x = 0.025, 0.05$ and 0.15 samples. These calculated BVS values signifies the average effect of the charge with the substitution around

the A–O₁₂ and B–O₆ polyhedra. Since, the substitution of Sr and Nb changes the average valency on the A (v_A) and B (v_B) sites, but to maintain the charge neutrality a charge transfer occurs between the A and B sites. The charge deficit for the each sample is calculated with the formula $\delta = 3 - (\langle v_A \rangle + \langle v_B \rangle)/2$, which directly correlates with the valence charge and termed as the non-stoichiometry. For $\delta \neq 0$, the valence charge at oxygen

Table 2. The strain parameter is $e_t = (c_{pc} - a_{pc})/(c_{pc} + a_{pc})$. c_{pc} and a_{pc} are the pseudocubic lattice constants given by $c/\sqrt{12}$ and $a/\sqrt{2}$. The distortion parameter Δ_d for the La–O polyhedra. The ϕ_1 is the tilting angle about the z-axis for BO_6 octahedra. The average bond valence sum (BVS) for the B and A sites are v_B and v_A , respectively.

x (%)	c_{pc}/a_{pc}	e_t	ϕ_1	Δ_d	v_B	v_A
		×10 ⁻³	(deg)	×10 ⁻²		
2.5	0.98	-8	8.48	6.6	3.103	3.096
5	0.985	-7	7.7	5.5	3.103	2.996
15	0.99	-4.5	7.15	4.7	3.008	2.802

site would be $6 \pm \delta$ in the unit cell. We have calculated the saturated bond lengths, below this coordination polyhedra cannot occupy more charge. The saturated bond valence (ν_s) can be calculated using $\nu_s = e^{(R_0 - R_s)/b}$, where R_s is the saturated bond valence parameter. The difference between the measured and saturated valence can be calculated, which gives the total valence deviation $\Delta\nu = \Delta\nu_{A-S} - \Delta\nu_{B-S}$ and demonstrates the balancing of the valence charge between the B–O₆ and A–O₁₂ polyhedra and vice-versa. We have plotted $\Delta\nu$ with the substitution concentration (not shown) and a linear fit of this curve crosses the $y = 0$ axis near the $x = 0.12$ value (i.e. around x equal to 12% concentration). This means that for $x > 0.12$, coordination polyhedra of A and B declines equally from the saturation. The estimated value of δ is found to be positive (about 0.09) only for the $x =$

0.15 sample. On the other hand, Brown and Shannon tested and reported that the bond valence method has accuracy around 5-7% for ionic compounds [41]. These obtained parameters from the structural analysis (particularly Co–O length and larger Co–O–Co angle) influence the magnetic properties of these samples [42, 43].

B. Magnetization and magnetic susceptibility

In order to study the magnetic behavior, we have performed isothermal magnetization (M–H) measurements at 5 K with variation of applied magnetic field upto ± 70 kOe, the M–H loops for all the samples are presented in Figures 3 (a–d) where the inset in each panel shows the zoomed view of M–H close to zero field. Re-

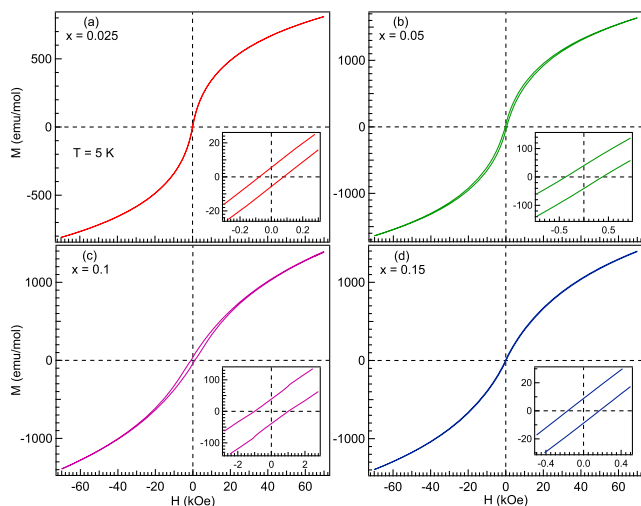


Figure 3. Isothermal magnetization (M–H) data for the $\text{La}_{(1-2x)}\text{Sr}_{2x}\text{Co}_{(1-x)}\text{Nb}_x\text{O}_3$ samples, (a) $x = 0.025$, (b) $x = 0.05$, (c) $x = 0.1$, and (d) $x = 0.15$, measured at 5 K, inset in each panel shows the magnetic behavior near origin.

cently, we observed the maximum value of magnetization ~ 170 emu/mol for the parent ($x = 0$) sample at highest applied magnetic field with the coercivity value of 1.35 kOe [7]. On the other hand, here as we increase the concentration of co-substitution gradually, the maximum magnetization increased to ~ 800 emu/mol (for the $x = 0.025$), but the hysteresis is almost disappeared; [see Figure 3(a)]. Further, for the $x = 0.05$ sample the magnetization increases to ~ 1600 emu/mol, which is around ten times higher than that of the $x = 0$ sample. For the $x = 0.1$ sample this value found to be ~ 1400 emu/mol and concurrently an increase in the hysteresis. Further, for the $x = 0.15$ sample there is no change in the magnetization value (~ 1400 emu/mol), but the hysteresis found to be negligible. It is interesting to note that there is a large increase in the magnetization with co-substitution

of Sr and Nb in 2:1 ratio, where we expect the Co ion maintains 3+ valence state like in the parent ($x = 0$) sample. In LaCoO_3 , an increase in the average Co–O bond length of the CoO_6 octahedra promote a spin-state transition from LS to IS state [30]. In the present case this behavior is evident as Co–O distance increases with the co-substitution in comparison to the $x = 0$ sample and this favors the possibility of similar spin-state transition. Although the nearest Co ions in IS state can interact ferromagnetically through the $e^1\text{-O-}e^0$ superexchange, as described in ref. [44]; however, the substitution of Nb ions, which act as the magnetic dilution in the system, decreases the probability of long-range magnetic ordering in the system. Also, only about 50% Co ions are in IS state, discussed later. The cumulative effect of these interactions reflects in the M–H curves, where first coercivity increases up to $x = 0.1$ sample and then decreases for the $x = 0.15$ sample. This is consistent as this Nb concentration is found to be close to the percolation limit, also found in the BVS results, for the magnetic dilution.

For further understanding the magnetic susceptibility and possible spin states of Co ion, we have studied the temperature dependence of the magnetization $M(T)$ by performing the measurements in the zero-field cooled (ZFC) and field cooled (FC) modes in the temperature range of 5–380 K [see Figures 4(a–d)]. We observe that

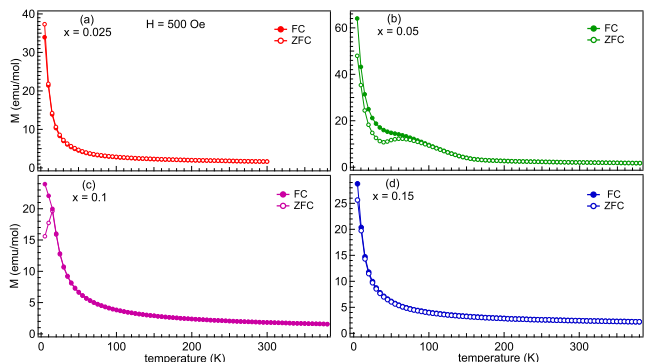


Figure 4. Temperature dependent ZFC–FC curves for the $\text{La}_{(1-2x)}\text{Sr}_{2x}\text{Co}_{(1-x)}\text{Nb}_x\text{O}_3$ samples, (a) $x = 0.025$, (b) $x = 0.05$, (c) $x = 0.1$, and (d) $x = 0.15$, measured at 500 Oe field.

there is no bifurcation between ZFC–FC curves, but a sharp increase in the magnetization below ~ 10 K temperature is clearly present for the $x = 0.025, 0.15$ samples. This behavior suggest the presence of Curie-Weiss paramagnetic behavior and/or surface related magnetism, which dominates in the low temperature regime and suggest the absence of long-range ordering in these samples [44]. On the other hand, the $M(T)$ data for the $x = 0.05$ sample exhibit a bifurcation between ZFC–FC curves below 80 K, and a cusp in the ZFC curve near 40 K and then the magnetization increases sharply to ~ 60 emu/mol. For the $x = 0.1$ sample, we observe a bifurcation be-

low 15 K and the ZFC magnetization decreases while FC increases at lower temperatures. The observed unconventional behavior in the magnetization for the $x = 0.05$ sample could be due to the presence of temperature induced spin-state transition, as observed for the parent sample LaCoO_3 [45]. The bifurcation between the FC and ZFC magnetization curves for the $x = 0.05$ and 0.1 samples indicate the possible presence of spin-glass phase [46], which further investigated using ac-magnetic susceptibility measurements (discussed later). We have analyzed the χ^{-1} vs. T curves of all the samples in the range of 220 to 380 K [see Figures 5 (a, b)] by the Curie-Weiss law using the following equation

$$\chi^{-1} = \frac{3k_B}{\mu_{\text{eff}}^2} (T - \theta_{\text{CW}})$$

and evaluated the effective magnetic moment (μ_{eff}) and the Curie-Weiss temperature (θ_{CW}) [7].

Within the approximation of only spin magnetic moment, average spin (S_{av}) is calculated from the experimentally observed values with the formula $\mu_{\text{eff}} = 2\sqrt{S(S+1)}$, which was resultant of different spin state contributions of Co ions. The values obtained from the analysis are presented in Table 3 with the different combination of spin states of Co, responsible for the magnetization present in the system. Note that the spin state of Co^{3+} can be preserved in intermediate and high spin-states in the 50:50 ratio, as was reported for the parent sample [7, 47]. Thus co-substitution of Sr and Nb in the

Table 3. Experimentally determined fitting parameters, Curie constant (C) in emu K mol^{-1} , effective magnetic moment (μ_B) and calculated average spin (S_{av}) for $\text{La}_{(1-2x)}\text{Sr}_{2x}\text{Co}_{(1-x)}\text{Nb}_x\text{O}_3$ samples.

x	$\theta_{\text{CW}} (K)$	C	$\mu_{\text{eff}} (\text{exp})$	$S_{\text{av}} (\text{exp})$
0	-220	1.85	3.85	1.50
0.025	-264	1.84	3.84	1.49
0.05	-157	1.89	3.88	1.51
0.1	-155	1.68	3.66	1.4
0.15	-465	3.73	5.46	2.3

LaCoO_3 preserves the valence states and spin-states at least up to the $x = 0.1$ sample. It is consistent as even small amount of Co^{2+} enhance the μ_{eff} significantly from $\approx 3.85 \mu_B$ to $4.65 \mu_B$ [7], which is not the case here up to $x = 0.1$ sample. On the other hand, it is interesting to note that the magnetization is significantly enhanced (see Figure 3) as compared to the parent sample [7]. This found to be unconventional and justify the need to further investigate the local structure and magnetism using absorption spectroscopy and magnetic circular dichroism studies at synchrotron radiation facility. However, the observed large value of μ_{eff} for the $x = 0.15$ sample can be due to the Nb concentration as it is near the percolation limit and can induce Co^{2+} valence states. It is

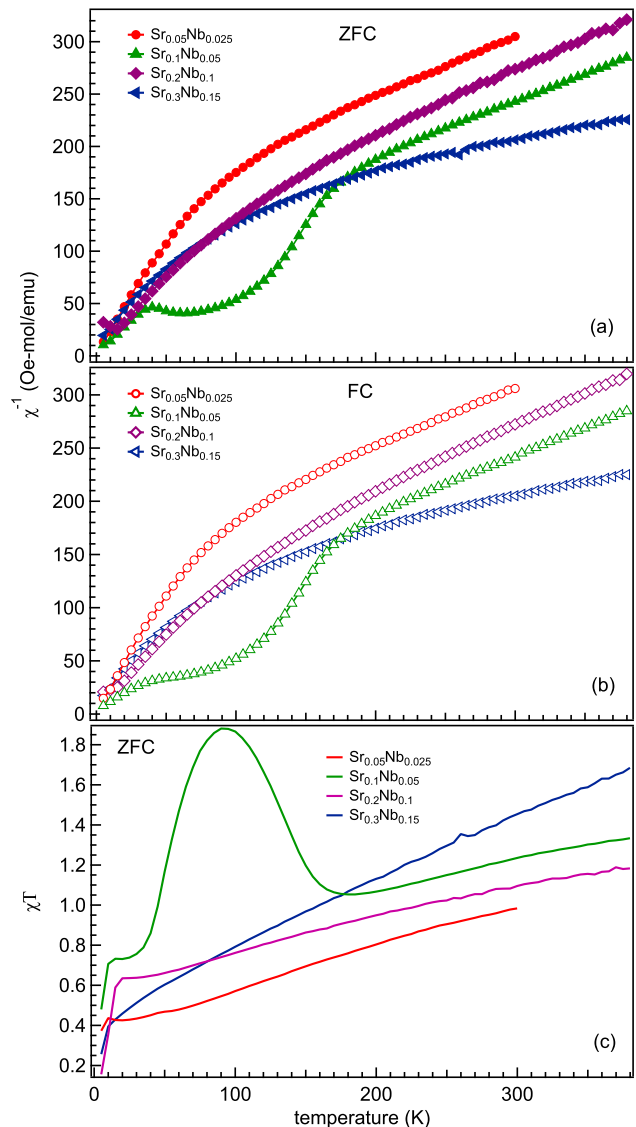


Figure 5. The χ^{-1} plots for the $\text{La}_{(1-2x)}\text{Sr}_{2x}\text{Co}_{(1-x)}\text{Nb}_x\text{O}_3$ samples as a function of temperature in (a) ZFC and (b) FC modes, and (c) the plot between χT (ZFC) vs temperature for all the samples.

also found from the BVS calculations that $x \geq 0.12$ will be overcharged. In the $\chi \cdot T$ vs. temperature plots; see Figure 5(c), we found that all samples manifest a linear behavior and then sharp decrease below 10 K, whereas for the $x = 0.05$ sample a broad peak centred ~ 80 K is observed. Interestingly, Androulakis *et al.* observed a very similar behavior in the parent LaCoO_3 sample with the application of magnetic field (0.1 Tesla) [45]. Interestingly, the authors found an evidence of ferromagnetic and antiferromagnetic interactions along with spin state transition at low temperatures [45]. The observed downturn in χ^{-1} vs. T curves [Figures 5(a, b)] at around 80 K [a broad peak in Figure 5(c)] in the $x = 0.05$ sample in-

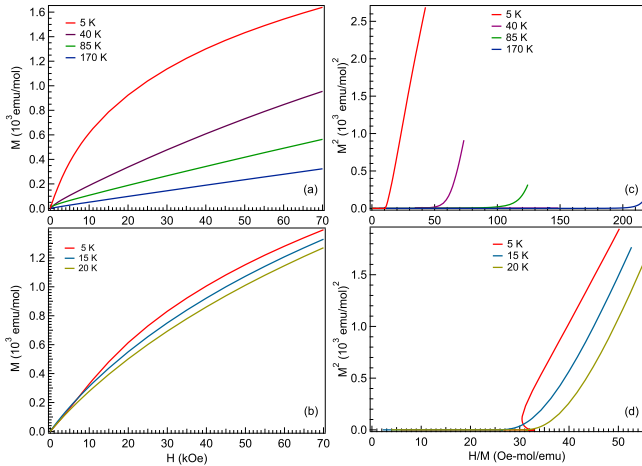


Figure 6. (a, b) The virgin curves (M-H) and (c, d) Arrott plots (M^2 vs H/M) of (a, c) $x = 0.05$, and (b, d) $x = 0.1$ samples, at different temperatures across the transition.

indicate a spin-state transition and presence of magnetic interactions at low temperatures [45].

Therefore, in order to probe the magnetic behavior across the bifurcation observed in the ZFC-FC data, we have measured the virgin curves (M vs. H) across the transition at various temperatures and plotted Arrott plots (M^2 vs. H/M) for $x = 0.05$ and 0.1 samples, as shown in Figures 6(a-d). From these M^2 vs. H/M curves, by fitting the high-field region with the straight line, which if have an intercept on the y-axis indicates a ferromagnetic interaction and a non-ferromagnetic interaction when an intercept on the x-axis. In these samples a linear fit gives an intercept on the x-axis for all samples which suggest a non-ferromagnetic interaction in the system, which is consistent with the M-H curves showing a non-saturating nature upto ± 70 kOe. Recently, we have observed that in LaCoO_3 , Nb substitution at Co site promotes short range ordering in the system for a large range of substitution ($x \leq 0.2$) [7, 47], and decreases the electrical conductivity as well. However, it has been reported that Sr substitution at La site induces the long range ordering in the system, an insulator to metal transition for $x = 0.18$ and a metallic ground state for $x \geq 0.2$ [30]. In the present case the Curie-Weiss temperatures are negative indicating antiferromagnetic interactions, whereas a small hysteresis in the isothermal magnetization curves indicate weak ferromagnetism along with the non-saturating behavior is a consequence of the antiferromagnetic interaction. This behavior suggests the coexistence of antiferromagnetic and ferromagnetic ordering and competition between them with co-substitution of Sr and Nb in LaCoO_3 . This is consistent as the Co-O-Co bond angle (γ) values extracted from the neutron diffraction (see Table I) are slightly larger than

the critical value $\gamma_c \approx 163^\circ$ for LaCoO_3 . The larger values of γ in the present case is favorable for the presence of magnetism in these samples [42, 48] probably due to internal strain as also the case in nanoparticles and thin films of LaCoO_3 [43, 49].

C. ac-magnetic susceptibility

Further we performed ac-susceptibility measurements for the $x = 0.05$ and 0.1 samples. In Figures 7(a, b), we present the ac-susceptibility data for the $x = 0.05$ sample, which show peaks centered at ≈ 15 K for both in-phase (dispersion) and the out of phase (absorption) terms. The peak position in each curve termed as freezing temperature (T_f), which is generally defined as a point where thermally activated processes achieve a maximum value. We observe that the peak position shifts ≈ 2 K towards the higher temperature with increase in the frequency from 19 to 4987 Hz. For the $x = 0.1$ sample, ac-susceptibility curves show a broad cusp below 18 K in the real and imaginary parts [see Figures 7(c, d)], which also shifts towards higher temperature and the magnitude of the magnetic moment decreases with the increase in the excitation frequency. This shift in the peak position of ac-susceptibility is a characteristic feature to the presence of spin glass (SG) behavior in the system [50]. The change in the magnitude of the moment indicates that the individual spin dynamics gets affected due to the excitation frequency. This cusp in the ac-susceptibility curve of $x = 0.1$ sample, matches with the bifurcation in the temperature dependent ZFC-FC curve of dc-magnetization [see Figure 4(c)].

We have performed detailed analysis of ac-susceptibility data to find the information about spin dynamics. The comparison of the change in T_f with the excitation frequency is generally termed as the frequency sensitivity, also termed as the Mydosh parameter [51] and can be calculated using the following formula

$$\delta T_f = \frac{\Delta T_f}{T_f(\Delta \log_{10} f)}$$

where f is excitation frequency. Here we have determined the difference employing the highest and lowest measured excitation frequencies. The obtained $\delta T_f = 0.05$ and 0.04 for the $x = 0.05$ and 0.1 samples, respectively. The values of δT_f are generally defined in the range of 0.004 – 0.018 for the canonical SG behavior, and for superparamagnets (SPMs) in between 0.3 – 0.5 [51, 52]. We have obtained values larger than the canonical spin glasses, such as CuMn ($\delta T_f = 0.005$) [51] and smaller than the SPMs (ideal non-interacting spin glasses), like holmium borate glass $\text{a-[Ho}_2\text{B}_3(\text{B}_2\text{O}_3)]$ [51]. The freezing temperature dependence on the excitation frequency strongly depends on the strength of interaction between the individual spins

or magnetic entities. For example, stronger frequency sensitivity means the weak interaction like in magnetic clusters, while smaller value means a strong interaction between individual spins in the system. For the systems having the strong interaction (like normal ferromagnetic and antiferromagnetic), large excitation frequencies (in range of MHz to GHz) are required to observe any remarkable shift in the frequency dependent ac-curves [53]. Thus, we can say that for $x = 0.1$ sample, spin interaction is relatively stronger owing to the smaller value of δT_f and that can be also seen in the sharp bifurcation in the dc-magnetization curve [see Figure 4(c)].

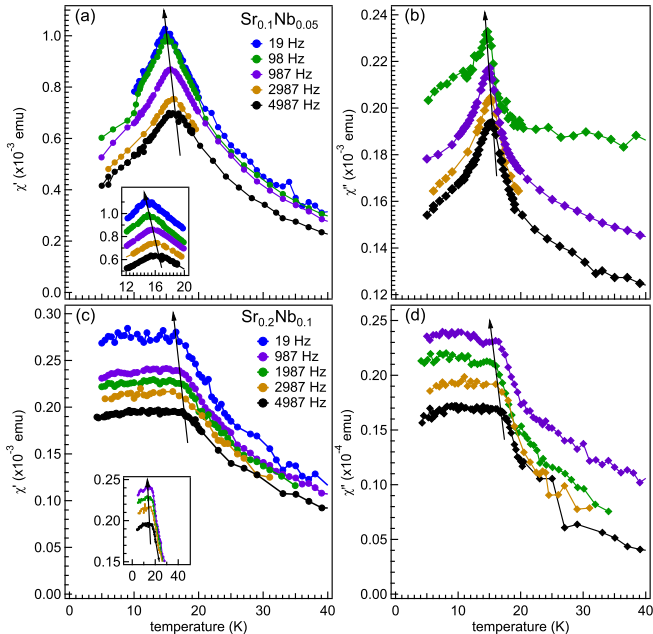


Figure 7. Temperature dependent ac-susceptibility measurements (a, c) real part, and (b, d) imaginary parts of the $x = 0.05$ and 0.1 samples, respectively; inset in (a) shows the shift in the peak position with the change in the frequency and inset in (c) shows that the susceptibility decreases after the freezing temperature T_f .

Frequency dependence of the freezing temperature T_f obtained from the real part, can be analyzed using the critical slowing down of the relaxation time by applying the standard dynamical scaling theory using the relation [51, 54],

$$\tau = \tau_0 \left(\frac{T_f - T_{SG}}{T_{SG}} \right)^{-z\nu'}$$

where τ is the relaxation time for the measured frequency, τ_0 is the characteristic relaxation time for the spin flipping or microscopic relaxation time, T_{SG} is the critical temperature for spin glass ordering or called static freezing temperature, i.e., when ν tends to zero, and $z\nu'$ is the dynamic exponent (in this ν' is the parameter for the correlation length $\zeta = (T_f - T_{SG})^{-\nu'}$ and $\tau \sim \zeta^z$). Such kind

of higher values have been observed elsewhere in SG and re-entrant spin glass (RSG) [51]. For the simplicity we can write this formula in the form of

$$\log_{10}(\tau) = \log_{10}(\tau_0) - z\nu' \log_{10} \left(\frac{T_f - T_{SG}}{T_{SG}} \right)$$

For further analysis we have plotted the data $\log_{10}(\nu)$ vs $\log_{10}[(T_f - T_{SG})/T_{SG}]$, where $\nu = 1/\tau$, in the Figure 8 (a), which show the linear behavior for both the samples ($x = 0.05$ and 0.1) and the values of τ_0 and $z\nu'$ can be found from the intercept and slope, respectively. We obtained $\tau_0 = 8.95 \times 10^{-7}$ s and 1.2×10^{-6} s, and $z\nu' = 2.7$ and 2.3 , for the $x = 0.05$ and 0.1 samples, respectively. It is previously reported that the conventional spin glasses have the value of τ_0 in the range of 10^{-12} – 10^{-14} s and $z\nu'$ lies between 4–12 [51, 55]. In comparison to this range τ_0 is larger and that indicates towards slower spin dynamics in our system, due to the presence of strong correlation between the individual spins rather than the single non-interacting spins.

This interaction of spins can be further investigated by the Arrhenius relation; because failure of Arrhenius law confirms the presence of interaction between the individual spins as it applies for the non-interacting or weakly interacting magnetic entities. Arrhenius relation can be written as

$$\nu = \nu_0 \exp \left(\frac{-E_a}{k_B T_f} \right)$$

where k_B is the Boltzmann constant, ν_0 is the characteristic attempt frequency, and E_a is the average thermal activation energy of the relaxation barrier. Arrhenius law accounts for the time scale to overcome the energy barriers by the activation process. In the plot of $\ln(\nu)$ versus $1/T_f$ (not shown), we found that the behavior is not linear towards the lower values of excitation frequencies, which also suggests the interaction of individual spins in the freezing process of the system. The fit of these values gives the unphysical outputs ($E_a/k_B = 700 \pm 75$ K and 1062 ± 190 K and $\nu_0 = 1.7 \times 10^{22}$ Hz and 2.6×10^{29} Hz for the $x = 0.05$ and 0.1 , respectively), that is due to the smaller number of fitting parameters and signifies the failure of Arrhenius law.

Now, to increase the number of fitting parameters, another law is more phenomenological to explore the dynamical scaling behavior of spin freezing is the Vogel-Fulcher(VF) law defined with an empirical relation

$$\nu = \nu_0 \exp \left(\frac{-E_a}{k_B (T_f - T_0)} \right)$$

where T_0 is the characteristic temperature or Vogel-Fulcher temperature used to measure interaction strength between magnetic entities, ν_0 , and E_a have the same physical meaning as defined previously. We fitted our data taking two methods first via fixing the previously

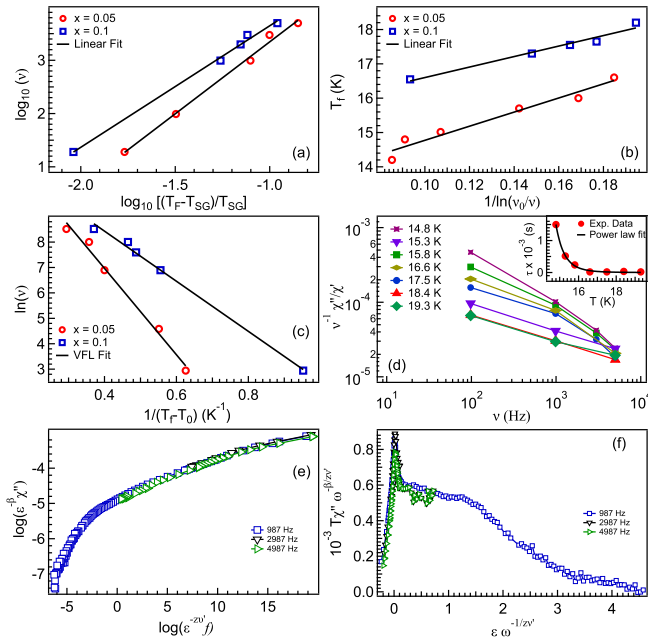


Figure 8. (a) Frequency sensitivity of the freezing temperature is plotted in terms of $\log_{10}(\nu)$ vs $\log_{10} \frac{T_f - T_{SG}}{T_{SG}}$, where $\nu = 1/\tau$, solid line shows the fit to the power law, (b) Excitation frequency dependence of freezing temperature is plotted as T_f vs $1/\ln(\nu_0/\nu)$, solid line is fit to Vogel-Fulcher law, (c) frequency dependence of T_f plotted as $\ln(\nu)$ vs $1/(T_f - T_0)$ along with a fit to the Vogel Fulcher law, and (d) temperature dependent Ogielski plot for the $x = 0.05$ sample (inset shows the power law fit of extracted frequency independent values.) (e) Critical slowing down analysis of the imaginary part of the $ac\text{-}\chi$ data at different frequencies, and (f) a linear scaling plot of $\chi''(\omega, T)/\omega^{\beta/z\nu'}$ plotted with $\epsilon/\omega^{1/z\nu'}$ using $\chi''(T)$ data, for the $x = 0.05$ sample.

obtained value of ν_0 , and in order to fit the data it is convenient to write the equation in terms of

$$\ln\left(\frac{\nu_0}{\nu}\right) = \frac{E_a/k_B}{(T_f - T_0)}$$

and that can be rearranged to

$$T_f = \frac{E_a/k_B}{\ln(\nu_0/\nu)} + T_0$$

A plot between T_f vs $1/\ln(\nu_0/\nu)$ allows us to determine the E_a/k_B and ν_0 from the slope and intercept, respectively [see Figure 8(b)]. Fit results give the values of $E_a/k_B = 20.5$ K and 15.3 K, and $T_0 = 12.7$ K and 15.1 K, for the $x = 0.05$ and 0.1 samples, respectively. In order to make sure these output fitting parameters as a result of fixing the ν_0 parameter are correct, we have also fitted the data fixing the T_0 parameters. This Vogel-Fulcher temperature (T_0) is determined by the method suggested by Souletie and Tholence [56] and obtained 13.5 ± 0.3 and

16 ± 0.2 K, for $x = 0.05$ and 0.1 , respectively. We used simplified relation

$$\ln(\nu) = \ln(\nu_0) - \frac{E_a/k_B}{T_f - T_0}$$

and plotted a curve between $\ln(\nu)$ versus $1/(T_f - T_0)$, where the best fit of data give value of characteristic relaxation time $\tau_0 = 1.1 \times 10^{-6}$ and 4.2×10^{-6} s, and activation energy $E_a/k_B = 17 \pm 1$ and 10 ± 0.5 K for the $x = 0.05$ and 0.1 samples, respectively [see Figure 8(c)]. From the above analysis, we determine that T_0 is nonzero for our system and that arises because of the interaction between the individual spins, which can be considered as a behavior of cluster-spin glass [57–59]. As we found that the value of T_0 is close to the freezing temperature, suggests the presence of Ruderman-Kittel-Kasuya-Yosida (RKKY) interaction. Using the Tholence criterion [60] $\delta T_h = (T_f - T_0)/T_f$, where T_f is measured at smallest excitation frequency, we obtained $\delta T_h = 0.07$ and 0.06 for the $x = 0.05$ and 0.1 samples, respectively. These values are comparable to the RKKY spin glass systems (e.g., 0.07 for the CuMn system) [60], and that suggest that our system falls in the category of RKKY spin glass. It is important to note here that the RKKY interactions are normally present in metallic systems and cannot present in band insulators. However, Hellman *et al.* reported spin-glass freezing with mixed antiferromagnetic and ferromagnetic interactions, and RKKY interaction in amorphous Gd-Si alloys, which are insulating or bad metallic, but nor band insulator [61, 62]. The nature of RKKY-type indirect exchange mediated by high density of electrons, localized due to disorder where the variation of the density of states $N(E)$ across the metal insulator transition may play crucial role [61, 63]. Interestingly, Andrulakis *et al.* proposed that a few existing itinerant electrons in LaCoO_3 can couple ferromagnetically via short range RKKY interactions at low temperatures [45]. In this context note that the $\text{La}_{(1-2x)}\text{Sr}_{2x}\text{Co}_{(1-x)}\text{Nb}_x\text{O}_3$ samples show insulating nature, but not a band insulator [45, 64] and it is consistent for the $x = 0.05$ sample where we observed larger value of $N(E)$ from resistivity analysis, discussed later. This analysis motivates for further experimental and theoretical studies on LaCoO_3 .

We found that the value of τ_0 obtained from the power law is one order of magnitude smaller than obtained from the VF law for the $x = 0.05$, whereas for the $x = 0.1$ both values are comparable. Further, in the frame of VF model, when $T_0 > E_a/k_B$ indicates a strong coupling, while $T_0 < E_a/k_B$ signifies the weak coupling between magnetic entities [65]. For our case as observed prior $x = 0.1$ has strong coupling in comparison to $x = 0.05$, sample. To further understand the spin glass dynamics we analyzed the data according to the formalism proposed by Ogielski [39], $\lim_{\nu \rightarrow 0} \chi''(\nu)/\chi'(\nu) = \tau_{av}$, where τ_{av} is the average correlation time. We have plotted $\nu^{-1}(\chi''/\chi')$ vs ν in the log-log scale near the T_f in the

Figure 8(d). At a given value of T , as depicted above we get a frequency independent value of $\nu^{-1}(\chi''/\chi')$ in lower frequency limit. This frequency independent value is estimated by extrapolating each curve up to the lowest excitation frequency ($\nu = 9$ Hz). Fitting the values extracted from the low frequency limit results the $\tau_0 = 1.5 \times 10^{-7}$ s, $T_{SG} = 11.5$ K. The value of τ_0 for the $x = 0.05$ sample is comparable to the calculated previously, which confirms that the spin dynamics is slower than expected for the typical SG systems.

For the dynamical scaling of the imaginary part of ac-susceptibility, two exponents $z\nu'$ and β are used and we followed the scaling formulation given below [66, 67],

$$\chi''(f, T) = \epsilon^\beta F(f\epsilon^{z\nu'})$$

where F is the universal scaling function, $\epsilon = (T - T_{SG})/T_{SG}$, and β is the order parameter. In Figure 8(e), we present the dynamical scaling for $x=0.05$ sample, where all the curves fall on the same line with the values of $z\nu' = 8.5$ and $\beta = 0.5$. For the further verification of these values with the theory, we have also plotted in Figure 8(f) the other scaling equation [68, 69] in terms of

$$T\chi''(\omega, T)/\omega^{\beta/z\nu'} = G(\epsilon/\omega^{1/z\nu'})$$

where G is the scaling function, which is expected to highlight any departures from the scaling equation due to higher sensitivity of the abscissa and ordinate scales, and it resembles the plot of χ'' versus temperature curve for all frequencies merged to a single curve, see Figure 8(f).

D. Low temperature neutron study

Now for the detailed investigation of magnetic phase, we have performed neutron diffraction at 3 K, see Figures 9(a–c). Neither additional magnetic Bragg peaks nor enhancement in the intensity of fundamental nuclear Bragg peaks has been observed at 3 K [42], ruling out the presence of a ferromagnetic/antiferromagnetic ordering [70, 71]. Further, we carried out neutron depolarization study down to 3 K on the $x = 0.05$ and 0.15 samples [Figures 9(d, e)], where no depolarization of neutron beam was observed ruling out the presence of any FM domains/clusters.

E. Resistivity measurements

The parent sample LaCoO_3 shows an insulating ground state, which can be tuned towards the metallic state by substituting Sr at La site [30], whereas the substitution of Nb at Co site drives the system towards the insulating regime [37]. Here we study the effect of co-substitution on the transport properties. The resistivity

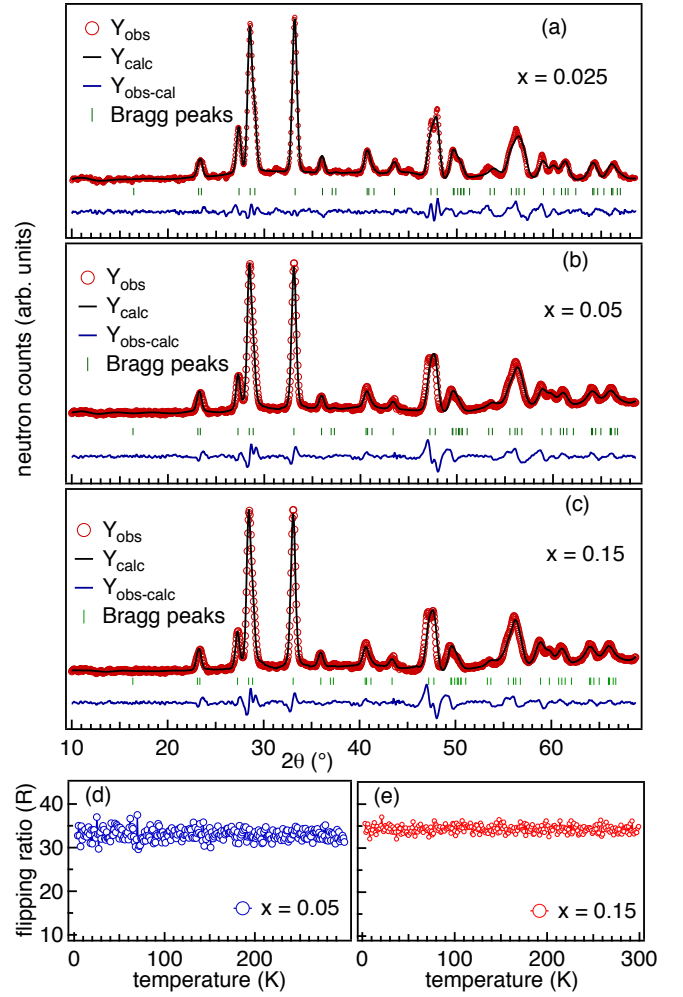


Figure 9. The Rietveld refined neutron powder diffraction data for the $\text{La}_{(1-2x)}\text{Sr}_{2x}\text{Co}_{(1-x)}\text{Nb}_x\text{O}_3$ samples, (a) $x = 0.025$, (b) $x = 0.05$, and (c) $x = 0.15$, measured at 3 K. (d) and (e) show the temperature variation of the flipping ratio (R) for $x = 0.05$ and 0.15, respectively.

data are presented in Figure 10. The electrical resistivity data show that all the samples are insulating and the resistivity increases from $\Omega\text{-cm}$ to $\text{M}\Omega\text{-cm}$ when the temperature decreases from 380 K to low temperatures. The electrical resistivity at low temperatures could not be measured because of compliance limit of the measuring instrument and highly insulating nature of $x = 0.025$ and 0.15 samples. To explain the electrical conduction we have fitted the data with Arrhenius and variable range hopping (VRH) models in the high and low temperature regimes, respectively [7]. We use the localization length comparable to the La/Co–O bond length and estimated the value of density of states near the Fermi level $N(E_F)$ ($\text{eV}^{-1}\text{cm}^{-3}$) using the VRH model. The density of states decreases with x , this suggest that the samples are becoming more insulating in nature. The calculated

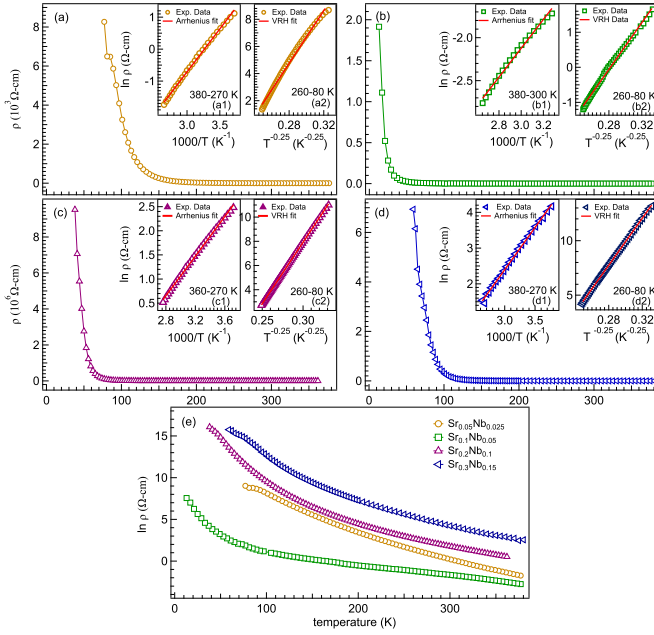


Figure 10. Temperature dependent resistivity data for the $\text{La}_{(1-2x)}\text{Sr}_{2x}\text{Co}_{(1-x)}\text{Nb}_x\text{O}_3$ samples (a) $x = 0.025$, (b) $x = 0.05$, (c) $x = 0.1$, and (d) $x = 0.15$, inset shows the fitting in different temperature ranges. (e) the comparison of resistivity values for all the samples in logarithmic scale.

Table 4. Calculated values of density of states $N(E)$ by VRH model fitting and activation energy E_a by Arrhenius equation fitting, and other fitting parameters for $\text{La}_{(1-2x)}\text{Sr}_{2x}\text{Co}_{(1-x)}\text{Nb}_x\text{O}_3$ samples.

samples $x(\%)$	VRH Model		Arrhenius Model
	$T_0(\text{K})$,	$N(E)(\text{eV}^{-1}\text{cm}^{-3})$	$E_a(\text{meV})$
0.025	8.9×10^7 ,	3.2×10^{20}	144 ± 3
0.05	1.2×10^6 ,	2.3×10^{22}	132 ± 2
0.1	1.1×10^8 ,	2.7×10^{20}	177 ± 2
0.15	1.4×10^8 ,	2.0×10^{20}	204 ± 2

values of the activation energy show that the insulating nature enhances with the increased substitution, and is in meV range [see Table IV], however, such small activation energy is expected to result in a semiconducting nature as it is in the case of LaCoO_3 with $E_a \approx 120$ meV [10]. We have calculated the value of activation energy as well as density of states near the Fermi level using the fitting parameters, as presented in the Table IV. Interestingly, for the $x = 0.05$ sample, the activation energy is significantly lower and $N(E_F)$ is also two order of magnitude higher than the other samples [9]. This makes it consistent with the observed signature of RKKY like interaction in this sample from ac-susceptibility analysis, as discussed earlier.

F. X-ray photoelectron spectroscopy study

We now move to the study of electronic properties of $x = 0.05$ and 0.1 samples using x-ray photoemission spectroscopy (XPS). The room temperature XPS core level spectra are presented in Figures 11 and 12. We observe that there is no significant shift in peak position within the limit of instrumental resolution. The Co $2p$ core level spectrum shows two main peaks, (corresponds to $2p_{3/2}$ and $2p_{1/2}$ at 779.5 eV and 795 eV, respectively) owing to the spin-orbit splitting of ~ 15.5 eV and an intensity ratio close to 2:1 [72, 73]. These observations confirm that the Co is predominantly in the Co^{3+} state, as reported for LiCoO_2 [74] and Na_xCoO_2 [75]. It also shows two loss features for each peak towards the higher binding energy (BE) side, known as the shake up satellites. The position of this satellite may suggest the presence of Co^{2+} ; however, if there is even 5% Co^{2+} present in the sample, the μ_{eff} increases from ≈ 3.85 to $4.65 \mu_B$ [7], which is significantly larger than what is observed from the magnetization measurements up to $x = 0.1$ sample, see table 3. Therefore, the formalism that the Co^{3+} valence state is preserved in LaCoO_3 , by co-substitution of Sr and Nb in 2:1 ratio, is consistent. In the transition metal oxides the satellite features can be explained with the charge transfer processes using molecular orbital theory or sudden approximation [76]. The ground state of Co^{3+} can be associated with a ligand (O^{2-} for the oxides) like $3d^6L$, where L is the highest occupied ligand shell i.e., $2p$ for the O^{2-} . After the photoexcitation d band lowers its energy and an electron is transferred from the ligand and that may lead to the satellite feature in Co $2p$ core-level.

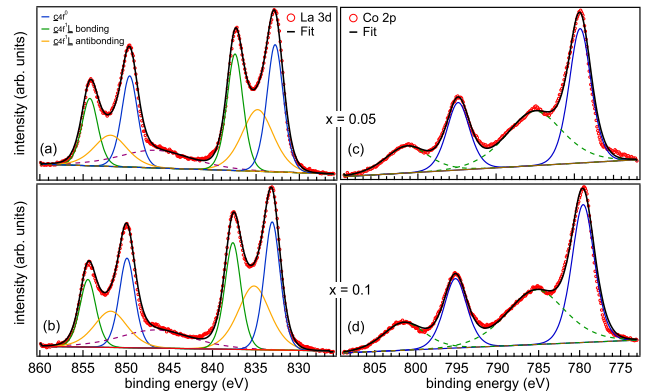


Figure 11. The La $3d$ (a, b) and Co $2p$ (c, d) core level photoemission spectra of $\text{La}_{(1-2x)}\text{Sr}_{2x}\text{Co}_{(1-x)}\text{Nb}_x\text{O}_3$ ($x = 0.05$ and 0.1) samples along with fitting components.

The La $3d$ spectrum shows four peaks [7], two peaks for each spin orbit component $3d_{5/2}$ and $3d_{3/2}$ along with two extra peaks due to the transfer of an electron from the oxygen valence band to the empty La $4f^0$ level [77]. The ionised La atoms have the $3d$ core level and $4f$ is the nearest unoccupied orbital, so a charge transfer from the

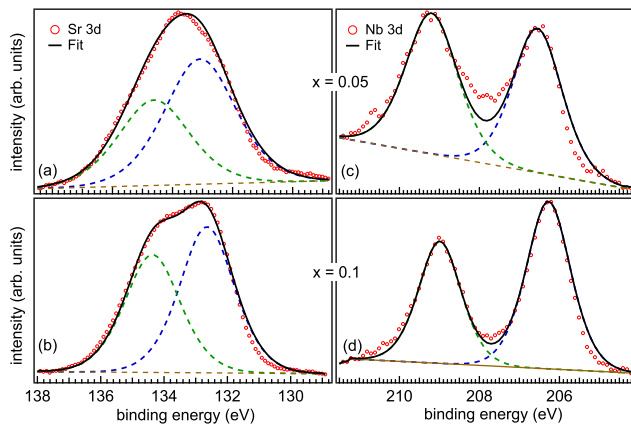


Figure 12. The core level photoemission spectra of substituted elements, Sr $3d$ (a, b) and Nb $3d$ (c, d) in $\text{La}_{(1-2x)}\text{Sr}_{2x}\text{Co}_{(1-x)}\text{Nb}_x\text{O}_3$ ($x = 0.05$ and 0.1) samples along with fitting components.

ligand valence band $\text{O}(2p)$ to the $4f^0$ orbital and transfer of an electron from the $3d$ core level to the continuum is believed a reason behind this complex structure [78, 79]. When we remove an electron from the core level we make the La ions more electronegative and then there is a possibility of electron withdrawal from the oxygen anions. Intensity of the observed satellite peaks depend on the electronegativity of the ligand molecule. For the fitting of La $3d$ core level spectra we follow the formalism used by Mullica *et al.* and hence each spin-orbit component is fitted with three components [78]. The main peaks at the lower binding energy (832.8 eV and 849.6 eV for the $3d_{5/2}$ and $3d_{3/2}$, respectively) corresponds to the final state without charge transfer, i.e., $3d^9 4f^0$ in La^{3+} and denoted by the $\underline{c}4f^0$, where \underline{c} denotes the presence of a core hole and $4f^0$ indicates absence of an electron in the $4f$ orbital. Other two peaks at the higher binding energies are bonding and antibonding of the final state denoted as $\underline{c}4f^1\underline{L}$, which indicates a charge transfer from $\text{O}(2p)$ ligand to the metal $4f$ orbital. The respective de-convoluted components are defined in Figure 11(a). It is important to note that unoccupied $4f$ orbital of the La^{3+} resides above the valence band; therefore an electron transfer to the $4f$ orbital will be an energy loss process [79, 80]. Figures 12 (a, b) show Sr $3d$ and Nb $3d$ core levels, which are fitted using Voigt function in CasaXPS software, after subtracting inelastic Tougaard background. The position of Sr $3d_{5/2}$ core level has been observed at 132.8 eV binding energy (BE) corresponds to the valency of $2+$, which is close to the reported in refs. [81, 82]. The Nb $3d$ core levels of both the samples are shown in Figures 12 (c, d), which clearly have spin orbit peaks $3d_{5/2}$ and $3d_{3/2}$ at 206.5 eV and 209 eV, respectively. This confirms the existence of Nb in the $5+$ valence state [7, 83].

CONCLUSIONS

In this study we have investigated the structural, magnetic, and electronic transport properties with the Sr/Nb co-substitution (hole as well as electron) in LaCoO_3 , i.e., $\text{La}_{(1-2x)}\text{Sr}_{2x}\text{Co}_{(1-x)}\text{Nb}_x\text{O}_3$. The recorded room temperature powder x-ray diffraction data are refined with rhombohedral symmetry, and no structural transition has been observed, but unit cell volume increases with x . The magnetization values increases significantly with respect to the $x = 0$ sample and the coercivity also changes. The calculated values of effective magnetic moment confirm the spin state of Co^{3+} in intermediate and high spin-states in the 50:50 ratio. The ac-susceptibility measurements show the change in T_f with the excitation frequency, which indicate spin-glass behavior in the system. The extracted relaxation time suggests slower spin dynamics, which confirms the cluster spin glass. Also, the Tholence criterion suggests the presence of RKKY interactions in $x = 0.05$ sample, which is consistent as the density of states are two order of magnitude larger in this case. The neutron diffraction and depolarization data provide a strong support at microscopic and mesoscopic length scales, respectively, to the observed spin-glass state. The dc-transport properties manifest that co-substitution drives the system towards insulating regime, and we extracted the activation energy and density of states. The x-ray photoemission measurements confirm that the Co ions predominantly exist in the $3+$ valence state and shakeup satellite features exists due to the ligand interaction. The La $3d$ core level spectra show a complex peak structure due to the electron transfer between the ligand and unoccupied $4f$ level. We also confirm the valence state of Sr and Nb as $2+$ and $5+$, respectively.

ACKNOWLEDGMENTS

RS gratefully acknowledge the DST-Inspire, India for fellowship. We would like to thank the research facilities: XRD, PPMS EVERCOOL-II at IIT Delhi. The powder neutron diffraction and ac-susceptibility measurements are supported under CRS project no. UDCSR/MUM/AO/CRS-M-270/2017/567. We thank Ploybussara Gomasang for help in the XPS measurements. The XPS measurements were supported by Sakura Science Program (aPBL), Shibaura Institute of Technology, under the Top Global University Project, Designed by Ministry of Education, Culture, Sports, Science and Technology in Japan. We also thank Vivek Anand, Priyanka, Mahesh Chandra, and Ajay Kumar for useful discussions and help. We thank SERB-DST for financial support through Early Career Research (ECR) Award (project reference no. ECR/2015/000159). Some facilities have been used in this study which are supported by BRNS through DAE Young Scientist Research

Award project sanction No. 34/20/12/2015/BRNS.

* rsdhaka@physics.iitd.ac.in

- [1] M. Abbate, J. C. Fuggle, A. Fujimori, L. H. Tjeng, C. T. Chen, R. Potze, G. A. Sawatzky, H. Eisaki, and S. Uchida, Electronic structure and spin-state transition of LaCoO_3 , *Phys. Rev. B* **47**, 16124 (1993).
- [2] M. A. Korotin, S. Yu. Ezhov, I. V. Solovyev, V. I. Anisimov, D. I. Khomskii, and G. A. Sawatzky, Intermediate-spin state and properties of LaCoO_3 , *Phys. Rev. B* **54**, 5309 (1996).
- [3] M. W. Haverkort, Z. Hu, J. C. Cezar, T. Burnus, H. Hartmann, M. Reuther, C. Zobel, T. Lorenz, A. Tanaka, N. B. Brookes, H. H. Hsieh, H.-J. Lin, C. T. Chen, and L. H. Tjeng, Spin state transition in LaCoO_3 studied using soft x-ray absorption spectroscopy and magnetic circular dichroism, *Phys. Rev. Lett.* **97**, 176405 (2006).
- [4] M. M. Altarawneh, G.-W. Chern, N. Harrison, C. D. Batista, A. Uchida, M. Jaime, D. G. Rickel, S. A. Crooker, C. H. Mielke, J. B. Betts, J. F. Mitchell, and M. J. R. Hoch, Cascade of magnetic field induced spin transitions in LaCoO_3 , *Phys. Rev. Lett.* **109**, 037201 (2012).
- [5] P. Augustinský, V. Křápek, and J. Kuneš, Doping induced spin state transition in LaCoO_3 : dynamical mean-field study, *Phys. Rev. Lett.* **110**, 267204 (2013).
- [6] B. Chakrabarti, T. Birol, and K. Haule, Role of entropy and structural parameters in the spin-state transition of LaCoO_3 , *Phys. Rev. M* **1**, 064403 (2017).
- [7] R. Shukla and R. S. Dhaka, Anomalous magnetic and spin glass behavior in Nb-substituted $\text{LaCo}_{1-x}\text{Nb}_x\text{O}_3$, *Phys. Rev. B* **97**, 024430 (2018).
- [8] A. Ishikawa, J. Nohara, and S. Sugai, Raman study of the orbital-phonon coupling in LaCoO_3 , *Phys. Rev. Lett.* **93**, 136401 (2004).
- [9] S. R. English, J. Wu, and C. Leighton, Thermally excited spin-disorder contribution to the resistivity of LaCoO_3 , *Phys. Rev. B* **65**, 220407 (2002).
- [10] C. Zobel, M. Kriener, D. Bruns, J. Baier, M. Grüninger, T. Lorenz, P. Reutler, and A. Revcolevschi, Evidence for a low-spin to intermediate-spin state transition in LaCoO_3 , *Phys. Rev. B* **66**, 020402(R) (2002).
- [11] S. Yamaguchi, Y. Okimoto, and Y. Tokura, Local lattice distortion during the spin-state transition in LaCoO_3 , *Phys. Rev. B* **55**, R8666 (1997).
- [12] T. Saitoh, T. Mizokawa, A. Fujimori, M. Abbate, Y. Takeda, and M. Takano, Electronic structure and temperature-induced paramagnetism in LaCoO_3 , *Phys. Rev. B* **55**, 4257 (1997).
- [13] D. P. Kozlenko, N. O. Golosova, Z. Jiráček, L. S. Dubrovinsky, B. N. Savenko, M. G. Tucker, Y. Le Godec, and V. P. Glazkov, Temperature and pressure-driven spin-state transitions in LaCoO_3 , *Phys. Rev. B* **75**, 064422 (2007).
- [14] R. P. Vasquez, X-ray photoemission measurements of $\text{La}_{1-x}\text{Ca}_x\text{CoO}_3$ ($x = 0, 0.5$), *Phys. Rev. B* **54**, 14938 (1996).
- [15] M. Kriener, C. Zobel, A. Reichl, J. Baier, M. Cwik, K. Berggold, H. Kierspel, O. Zabara, A. Freimuth, and T. Lorenz, Structure, magnetization, and resistivity of $\text{La}_{1-x}\text{M}_x\text{CoO}_3$ ($\text{M}=\text{Ca}, \text{Sr}, \text{and Ba}$), *Phys. Rev. B* **69**, 094417 (2004).
- [16] K. Sato, A. Matsuo, K. Kindo, Y. Hara, K. Nakaoka, Y. Kobayashi, and K. Asai, Field-induced spin-state transition in $\text{LaCo}_{1-x}\text{M}_x\text{O}_3$ ($\text{M} = \text{Al}, \text{Ga}, \text{Rh}, \text{and Ir}$), *J. Phys. Soc. Jap.* **83**, 114712 (2014).
- [17] S. V. Streltsov, V. V. Gapontsev, and D. I. Khomskii, Valence states and possible charge ordering in $\text{LaCo}_{1-x}\text{Rh}_x\text{O}_3$, *J. Phys.: Condens. Matter* **28**, 086005 (2016).
- [18] D. V. Karpinsky, I. O. Troyanchuk, K. Bärner, H. Szymczak, and M. Tovar, Crystal structure and magnetic ordering of the $\text{LaCo}_{1-x}\text{Fe}_x\text{O}_3$ system, *J. Phys.: Condens. Matter* **17**, 7219 (2005).
- [19] I. Á.-Serrano, G. J. Cuello, M. L. López, A. J.-López, C. Pico, E. R.-Castellón, E. Rodríguez, and M. L. Veiga, Magnetic behaviour governed by Co spin transitions in $\text{LaCo}_{1-x}\text{Ti}_x\text{O}_3$ ($0 \leq x \leq 0.5$) perovskite oxides, *J. Phys. D: Appl. Phys.* **41**, 195001 (2008).
- [20] K. Yoshii and H. Abe, Doping effects of Ru in $\text{La}_{0.5}\text{Sr}_{0.5}\text{CoO}_3$ ($\text{L} = \text{La}, \text{Pr}, \text{Nd}, \text{Sm}, \text{and Eu}$), *Phys. Rev. B* **67**, 094408 (2003).
- [21] D. Hammer, J. Wu, and C. Leighton, Metal-insulator transition, giant negative magnetoresistance, and ferromagnetism in $\text{LaCo}_{1-y}\text{Ni}_y\text{O}_3$, *Phys. Rev. B* **69**, 134407 (2004).
- [22] J. Baier, S. Jodlauk, M. Kriener, A. Reichl, C. Zobel, H. Kierspel, A. Freimuth, and T. Lorenz, Spin-state transition and metal-insulator transition in $\text{La}_{1-x}\text{Eu}_x\text{CoO}_3$, *Phys. Rev. B* **71**, 014443 (2005).
- [23] M. Kriener, M. Braden, H. Kierspel, D. Senff, O. Zabara, C. Zobel, and T. Lorenz, Magnetic and structural transitions in $\text{La}_{1-x}\text{A}_x\text{CoO}_3$ ($\text{A}=\text{Ca}, \text{Sr}, \text{and Ba}$), *Phys. Rev. B* **79**, 224104 (2009).
- [24] I. O. Troyanchuk, D. V. Karpinsky, and R. Szymczak, Possible ferromagnetic interactions between IS Co^{3+} ions in Nb doped cobaltites, *Phys. Stat. Sol. (b)* **242**, 49 (2005).
- [25] P. G. Radaelli and S. W. Cheong, Structural phenomena associated with the spin-state transition in LaCoO_3 , *Phys. Rev. B* **66**, 094408 (2002).
- [26] R. D. Shannon, Revised effective ionic radii and systematic studies of interatomic distances in halides and chalcogenides, *Acta Crystallogr., Sect. A* **32**, 751 (1976).
- [27] R. D. Shannon and C. T. Prewitt, Effective ionic radii in oxides and fluorides, *Acta Crystallogr. Sect. B* **25**, 925 (1969).
- [28] P. M. Raccach and J. B. Goodenough, Localized-electron to collective-electron transition in the system $(\text{La}, \text{Sr})\text{CoO}_3$, *J. Appl. Phys.* **39**, 1209 (1968).
- [29] T. Kyōmen, Y. Asaka, and M. Itoh, Negative cooperative effect on the spin-state excitation in LaCoO_3 , *Phys. Rev. B* **67**, 144424 (2003).
- [30] J. Wu and C. Leighton, Glassy ferromagnetism and magnetic phase separation in $\text{La}_{1-x}\text{Sr}_x\text{CoO}_3$, *Phys. Rev. B* **67**, 174408 (2003).
- [31] Ravi Prakash, Rishabh Shukla, Priyanka Nehla, Anita Dhaka, and R. S. Dhaka, Tuning ferromagnetism and spin state in $\text{La}_{1-x}\text{A}_x\text{CoO}_3$ ($\text{A} = \text{Sr}, \text{Ca}$) nanoparticles, *J. Alloys Compd.* **764**, 379 (2018).
- [32] M. A. Senaris-Rodríguez and J. B. Goodenough, Magnetic and transport properties of the system $\text{La}_{1-x}\text{Sr}_x\text{CoO}_{3-\delta}$ ($0 < x \leq 0.5$), *J. Solid State Chem.* **118**, 323 (1995).

- [33] M. Itoh, I. Natori, S. Kubota, and K. Motoya, Hole doping effect on magnetic properties of $\text{La}_{1-x}\text{Sr}_x\text{CoO}_3$ ($0 \leq x \leq 0.5$), *J. Magn. Magn. Mater.* **140**, 1811 (1995).
- [34] C. Zener, Interaction between the d shells in the transition metals, *Phys. Rev.* **81**, 440 (1951).
- [35] C. Zener, Interaction between the d-Shells in the transition metals. II. ferromagnetic compounds of manganese with perovskite structure, *Phys. Rev.* **82**, 403 (1951).
- [36] D. N. H. Nam, K. Jonason, P. Nordblad, N. V. Khiem, and N. X. Phuc, Coexistence of ferromagnetic and glassy behavior in the $\text{La}_{0.5}\text{Sr}_{0.5}\text{CoO}_3$ perovskite compound, *Phys. Rev. B* **59**, 4189 (1999).
- [37] V. Oygarden, H. L. Lein, and T. Grande, Structure, thermal expansion and electrical conductivity of Nb-substituted LaCoO_3 , *J. Solid State Chem.*, **192**, 246 (2012).
- [38] L. Pauling, The principles determining the structure of complex ionic crystals, *J. Amer. Chem. Soc.* **51**, 1010 (1929).
- [39] A. T. Ogielski, Dynamics of three-dimensional Ising spin glasses in thermal equilibrium, *Phys. Rev. B* **32**, 7384 (1985); P. Granberg, P. Svedlindh, P. Nordblad, L. Lundgren, and H. S. Chen, Dynamics of fluctuations in the ordered phase of kinetic Ising models, *Phys. Rev. B* **35**, 2075 (1987).
- [40] D. Altermatt and I. D. Brown, The automatic searching for chemical bonds in inorganic crystal structures, *Acta Cryst.* **B41**, 244 (1985).
- [41] I. D. Brown and R. D. Shannon, Bond-valence parameters obtained from a systematic analysis of the inorganic crystal structure database, *Acta Cryst.* **A29**, 266 (1973).
- [42] A. M. Durand, D. P. Belanger, C. H. Booth, F. Ye, S. Chi, J. A. Fernandez-Baca, and M Bhat, Magnetism and phase transitions in LaCoO_3 , *J. Phys.: Condens. Matter* **25**, 382203 (2013).
- [43] A. M. Durand, D. P. Belanger, T. J. Hamil, F. Ye, S. Chi, J. A. Fernandez-Baca, C. H. Booth, Y. Abdollahian, and M Bhat, The unusual magnetism of nanoparticle LaCoO_3 , *J. Phys.: Condens. Matter* **27**, 176003 (2015).
- [44] J. -Q. Yan, J. -S. Zhou, and J. B. Goodenough, Ferromagnetism in LaCoO_3 , *Phys. Rev. B* **70**, 014402 (2004).
- [45] J. Androulakis, N. Katsarakis, and J. Giapintzakis, Ferromagnetic and antiferromagnetic interactions in lanthanum cobalt oxide at low temperatures, *Phys. Rev. B* **64**, 174401 (2001).
- [46] H. Guo, K. Manna, H. Luetkens, M. Hoelzel, and A. C. Komarek, Spin glass behavior in $\text{LaCo}_{1-x}\text{Rh}_x\text{O}_3$ ($x = 0.4, 0.5, \text{ and } 0.6$), *Phys. Rev. B* **94**, 205128 (2016).
- [47] I. O. Troyanchuk, D. V. Karpinsky, and R. Szymczak, Spin state and magnetic interaction of cobalt ions in niobium-doped cobaltites, *Phys. Solid State*, **48**, 722 (2006).
- [48] D. P. Belanger, T. Keiber, F. Bridges, A. M. Durand, A. Mehta, H. Zheng, J. F. Mitchell, and V. Borzenets, Structure and magnetism in LaCoO_3 , *J. Phys.: Condens. Matter* **28**, 025602 (2016).
- [49] D. Fuchs, E. Arac, C. Pinta, S. Schuppler, R. Schneider, and H. v. Löhneysen, Tuning the magnetic properties of LaCoO_3 thin films by epitaxial strain, *Phys. Rev. B* **77**, 014434 (2008).
- [50] C. Sow, D. Samal, P. S. Anil Kumar, A. K. Bera, and S. M. Yusuf, Structural-modulation-driven low-temperature glassy behavior in SrRuO_3 , *Phys. Rev. B* **85**, 224426 (2012).
- [51] J. A. Mydosh, Spin glasses: an experimental introduction (Taylor and Francis, London), (1993).
- [52] N. Hanasaki, K. Watanabe, T. Ohtsuka, I. Kezsmarki, S. Iguchi, S. Miyasaka, and Y. Tokura, Nature of the transition between a ferromagnetic metal and a spin-glass insulator in pyrochlore molybdates, *Phys. Rev. Lett.* **99**, 086401 (2007).
- [53] A. Malinowski, V. L. Bezusyy, R. Minikayev, P. Dziawa, Y. Syryanyy, and M. Sawicki, Spin-glass behavior in Ni-doped $\text{La}_{1.85}\text{Sr}_{0.15}\text{CuO}_4$, *Phys. Rev. B* **84**, 024409 (2011).
- [54] M. Sasaki, P. E. Jönsson, and H. Takayama, Aging and memory effects in superparamagnets and superspin glasses, *Phys. Rev. B* **71**, 104405 (2005).
- [55] D. N. H. Nam, R. Mathieu, P. Nordblad, N. V. Khiem, and N. X. Phuc, Spin-glass dynamics of $\text{La}_{0.95}\text{Sr}_{0.05}\text{CoO}_3$, *Phys. Rev. B* **62**, 8989 (2000).
- [56] J. Souletie and J. L. Tholence, Critical slowing down in spin glasses and other glasses: fulcher versus power law, *Phys. Rev. B* **32**, 516(R) (1985).
- [57] K. Gunnarsson, P. Svedlindh, P. Nordblad, L. Lundgren, H. Aruga, and A. Ito, Dynamics of an ising spin-glass in the vicinity of the spin-glass temperature, *Phys. Rev. Lett.* **61**, 754 (1988).
- [58] V. K. Anand, D. T. Adroja, and A. D. Hillier, Ferromagnetic cluster spin-glass behavior in PrRhSn_3 , *Phys. Rev. B* **85**, 014418 (2012).
- [59] M. D. Mukadam, S. M. Yusuf, P. Sharma, S. K. Kulshreshtha, and G. K. Dey, Dynamics of spin clusters in amorphous Fe_2O_3 , *Phys. Rev. B* **72**, 174408 (2005).
- [60] J. L. Tholence, On the frequency dependence of the transition temperature in spin glasses, *Phys. B (Amsterdam)* **126**, 157 (1984).
- [61] F. Hellman, D. R. Queen, R. M. Potok, and B. L. Zink, Spin-glass freezing and RKKY interactions near the metal insulator transition in amorphous Gd-Si alloys, *Phys. Rev. Lett.* **84**, 5411 (2000).
- [62] E. Helgren, F. Hellman, L. Zeng, N. Sinenian, R. Islam, and D. J. Smith, Magnetic and transport properties of amorphous $\text{Gd}_x\text{Ge}_{1-x}$ alloys near the metal-insulator transition, *Phys. Rev. B* **76**, 184440 (2007).
- [63] L. Bokacheva, W. Teizer, F. Hellman, and R. C. Dynes, Variation of the density of states in amorphous GdSi at the metal-insulator transition, *Phys. Rev. B* **69**, 235111 (2004).
- [64] R. J. Radwanski, Z. Ropka, Strongly correlated crystal-field approach to Mott insulator LaCoO_3 , *Physica B* **359**, 1354 (2005).
- [65] S. Shtrikman and E. Wohlfarth, The theory of the Vogel-Fulcher law of spin glasses, *Phys. Lett. A* **85**, 467 (1981).
- [66] S. Geschwind, D. A. Huse, and G. E. Devlin, New approach to critical dynamic scaling in random magnets, *Phys. Rev. B* **41**, 4854 (1990).
- [67] N. Marcano, P. A. Algarabe, L. Fernández Barquín, J. P. Araujo, A. M. Pereira, J. H. Belo, C. Magén, L. Morellón, and M. R. Ibarra, Cluster-glass dynamics of the Griffiths phase in $\text{Tb}_{5-x}\text{La}_x\text{Si}_2\text{Ge}_2$, *Phys. Rev. B* **99**, 054419 (2019).
- [68] Y. Bitla, S. N. Kaul, and L. Fernández Barquín, Nonlinear susceptibilities as a probe to unambiguously distinguish between canonical and cluster spin glasses, *Phys. Rev. B* **86**, 094405 (2012).

- [69] S. Nair and A. K. Nigam, Critical exponents and the correlation length in the manganite spin glass $\text{Eu}_{0.5}\text{Ba}_{0.5}\text{MnO}_3$, *Phys. Rev. B* **75**, 214415 (2007).
- [70] V. Sikolenko, V. Efimov, E. Efimova, A. Sazonov, C. Ritter, A. Kuzmin, and I. Troyanchuk, Neutron diffraction studies of structural and magnetic properties of niobium doped cobaltites, *J. Phys.: Condens. Matter* **21**, 436002 (2009).
- [71] N. E. Rajeevan, Vinod Kumar, Rajesh Kumar, Ravi Kumar, S.D. Kaushik, Neutron diffraction studies of magnetic ordering in Ni-doped LaCoO_3 , *J. Magn. Magn. Mater.* **393**, 394 (2015).
- [72] A. Chainani, M. Mathew, D.D. Sarma, Electron-spectroscopy study of the semiconductor-metal transition in $\text{La}_{1-x}\text{Sr}_x\text{CoO}_3$, *Phys. Rev. B* **46**, 9976 (1992).
- [73] T. J. Chuang, C. R. Brundle, and D. W. Rice, Interpretation of the x-ray photoemission spectra of cobalt oxides and cobalt oxide surfaces, *Surf. Sci.* **59**, 413 (1976).
- [74] A. W. Moses, H. G. Garcia-flores, J. G. Kim, and M. A. Langell, Surface properties of LiCoO_2 , LiNiO_2 and $\text{LiNi}_{1-x}\text{Co}_x\text{O}_2$, *Appl. Surf. Sci.* **253**, 4782 (2007).
- [75] D. Jugovic, M. Milovic, M. Popovic, V. Kusigerski, S. Skapin, Z. Rakocevic, and M. Mitric, Effects of fluorination on the structure, magnetic and electrochemical properties of the P2-type Na_xCoO_2 powder, *J. Alloys Compd.* **774**, 30 (2019).
- [76] S. Hüfner, *Photoelectron spectroscopy; principles and applications*, ISBN 978-3-662-09280-4, (2nd edition), Springer, US, (1996).
- [77] D. J. Lam, D. W. Veal, and D. E. Ellis, Electronic structure of lanthanum perovskites with $3d$ transition elements, *Phys. Rev. B* **22**, 5730 (1980).
- [78] D. F. Mullica, C. K. C. Lok, H.O. Perkins, and V. Young, X-ray photoelectron final-state screening in $\text{La}(\text{OH})_3$: A multiplet structural analysis, *Phys. Rev. B* **31**, 4039 (1985).
- [79] A. J. Signorelli, and R. G. Hayes, X-ray photoelectron spectroscopy of various core levels of lanthanide ions: the roles of monopole excitation and electrostatic coupling, *Phys. Rev. B.* **8**, 81 (1973).
- [80] D. D. Sarma, P. V. Kamath, and C. N. R. Rao, Satellites in the x-ray photoelectron spectra of transition-metal and rare-earth compounds, *Chem. Phys.* **73**, 71 (1982).
- [81] S. de Jong, F. Masee, Y. Huang, M. Gorgoi, F. Schaeffers, J. Fink, A. T. Boothroyd, D. Prabhakaran, J. B. Goedkoop, and M. S. Golden, High-resolution hard x-ray photoemission investigation of $\text{La}_{2-2x}\text{Sr}_{1+2x}\text{Mn}_2\text{O}_7$ ($0.30 \leq x \leq 0.50$): microscopic phase separation and surface electronic structure of a bilayer colossal magnetoresistance manganite, *Phys. Rev. B.* **80**, 205108 (2009).
- [82] H. Guo, Y. Li, D. Urbina, B. Hu, R. Jin, T. Liu, D. Fobes, Z. Mao, E. W. Plummer, and J. Zhang, Doping and dimensionality effects on the core-level spectra of layered ruthenates, *Phys. Rev. B.* **80**, 205108 (2009).
- [83] A. Sasahara and M. Tomitori, XPS and STM Study of Nb-Doped $\text{TiO}_2(110)-(1 \times 1)$ Surfaces, *J. Phys. Chem. C* **117**, 17680 (2013).